Second-harmonic and linear optical spectroscopic study of silicon nanocrystals embedded in SiO$_2$

Junwei Wei, Adrian Wirth, and Michael C. Downer[*]

Department of Physics, The University of Texas at Austin, Austin, Texas 78712, USA

Bernardo S. Mendoza

Department of Photonics, Centro de Investigaciones en Optica, A. C. León, Guanajuato, Mexico

The optical second-harmonic generation (SHG) spectra of silicon nanocrystals (Si NCs) prepared by implanting Si ions uniformly into silica substrates, then annealing, are compared and contrasted to their ellipsometric and photoluminescence excitation (PLE) spectra. Three resonances—two close in energy to E_1 (3.4 eV) and E_2 (4.27 eV) critical-point resonances of crystalline silicon (c-Si), and a broad resonance intermediate in energy between E_1 and E_2—are observed in all three types of spectra. These features are observed in conjunction with a sharp 520 cm^{-1} Raman peak characteristic of c-Si. While the ellipsometric and PLE spectra differ only slightly between samples with average NC diameter $\langle d_{NC} \rangle = 3$ and 5 nm, the SHG spectrum changes dramatically from a nearly featureless spectrum dominated by the non-bulk-like intermediate resonance for $\langle d_{NC} \rangle = 3$ nm, like the SHG spectrum of amorphous Si (a-Si), to a featured spectrum with pronounced resonances at 3.4, 3.73, and 4.8 eV for $\langle d_{NC} \rangle = 5$ nm. The results suggest that SHG is uniquely sensitive to a nanointerfacial transition region containing a-Si and suboxide that is most prominent for small $\langle d_{NC} \rangle$, while ellipsometric and PLE spectra are more sensitive to the c-Si core of the NCs. The persistence of an a-Si tail in the Raman spectrum of annealed samples supports the interpretation.

PACS number(s): 78.67.Bf, 42.65.−k, 78.20.Ci, 73.22.−f

I. INTRODUCTION

Silicon nanocrystals (NCs) have opened possibilities for silicon photonics because of their efficient light emission at room temperature.[1–3] Si NCs embedded in amorphous SiO$_2$ have attracted particular attention because of their robustness and long-term stability. Despite progress in fabricating photonic devices from Si NCs,[3] the origin of the efficient photoluminescence (PL) and the structure of the elusive NC/SiO$_2$ interfaces remain controversial. The dependence of PL wavelength on NC size has been cited as proof that PL originates from bulk quantum confined (QC) states.[4] However, size dependence is less clear for smaller NCs (few nanometers in diameter) with large surface to volume ratio. Here NC/SiO$_2$ interfaces appear to play an active, if not dominant, role in PL.[5–8] Coordination defects,[9] NC interface chemistry,[10] Si-O bonds,[11] oxidation-induced defects,[7] interface strain,[12] and interfacial Si-O vibrations[13] have all been proposed as interface-mediated PL mechanisms. Indeed, PL transitions attributable to localized interfacial states have been clearly identified and classified in recent high-field magneto-PL experiments,[14] although identification of radiative recombination centers with specific interfacial structures remains controversial. Recent simulations[15,16] and x-ray Raman experiments[17] suggest that NC/SiO$_2$ interfaces, unlike the sharp interface between planar Si and SiO$_2$, consists of an extended region of amorphous Si (a-Si) and suboxides of variable composition, although recent x-ray photoelectron spectroscopy studies in conjunction with near-edge x-ray-absorption fine-structure spectroscopy have questioned this conclusion.[18]

Optical spectroscopy provides a powerful noninvasive tool for probing the structure of oxide-embedded Si NCs, including the active buried NC/SiO$_2$ interfaces. The latter are inaccessible to standard surface science techniques that utilize incident or emitted electrons because of the small penetration/escape depth of electrons. Steady-state PL studies reveal the important role of QC and surface/interface states in the process of photoluminescence.[7,11,13,14] Time-resolved PL makes it possible to distinguish between contributions from intrinsic NC-core and surface/interface states, since recombination at core and interface states occurs on different time scales.[19] Optical absorption spectra have elucidated the electronic structure of embedded Si NCs.[20] Spectroscopic ellipsometry (SE) has revealed a QC effect on the dielectric function.[21–26] Raman spectroscopy has determined nanostructure-related properties including elastic strain,[27] hydrostatic stress,[28] nonstoichiometric composition,[29] and core-shell structure.[27,28,30,31]

In this paper, we report a second-harmonic generation (SHG) spectroscopic study of Si NCs of average diameter $\langle d_{NC} \rangle = 3$ and 5 nm embedded in amorphous SiO$_2$, complemented by conventional spectroscopic studies mentioned above. SHG has been widely applied to planar interfaces for over 20 years because it is often sensitive to interfacial electronic structure and chemistry.[32–35] In centrosymmetric materials such as Si, bulk contributions are dipole forbidden, and thus appear only in quadrupolar order, while contributions from planar interfaces are dipolar. Nevertheless, dominance of planar interface dipole contributions is neither obvious *a priori* nor universal, because the volume contributing to the bulk quadrupole signal is much larger than the interface layer. Indeed for this reason early observations of reflected SHG from planar interfaces of centrosymmetric materials were attributed to the bulk quadrupolar response.[36] For polarization configurations in which both planar interface dipole and bulk quadrupole SHG signals are present, Sipe showed that a complete separation is impossible, since the isotropic bulk quadrupolar contribution always appears combined with the one of the surface dipolar contributions.[37] Consequently the distinguishing characteristics, and the frequent dominance, of planar interfacial contributions were established empirically

based on, e.g., contrasting dependence of interfacial and bulk contributions on sample rotation,[38] appearance of non-bulk-like resonances in the SHG spectrum,[39] and sensitivity of those resonances to interface modification.[39] Similar empirical tests, along with strategic choice of experimental geometry, have even enabled interface-specific SHG study of planar interfaces of noncentrosymmetric materials (e.g., GaAs),[40] for which bulk and interfacial contributions are of equivalent dipolar order.

SHG spectroscopy of embedded Si NCs faces a similar bulk/interface ambiguity, and relies similarly on empirical distinction. The phenomenological theory of SHG by nanospheres of centrosymmetric material was developed only in the past decade. Dadap *et al.* calculated SH scattering from a single centrosymmetric nanosphere excited by a plane wave in terms of nonlocally excited electric dipole and locally excited quadrupole polarizations.[41] Brudny *et al.* showed that an incident wave with transverse spatial variations gives rise to additional bulk and interfacial quadratic nonlinear responses.[42,43] Mochan *et al.* extended the analysis to a composite medium made up of a thin disordered array of centrosymmetric nanospheres.[43] The total second-harmonic (SH) response, after spatial averaging of interface nonlocal dipole and the bulk local quadrupole contributions, appears at quadrupolar order, but the theory provides no *a priori* guidance on whether bulk or interfacial contributions dominate. Thus, as with planar interfaces, SHG spectroscopy experiments and comparison to conventional spectroscopy are essential. Early SHG experiments on embedded Si NCs were performed with a single tightly focused incident beam at a single wavelength.[44] However, the weakness of the signal and the need to excite near the optical damage threshold of the embedded NCs inhibited spectroscopic studies. The development of a two-beam, cross-polarized SHG (XP2-SHG) geometry that is specifically tailored to observation of quadrupolar SHG[45,46] enabled a stronger SHG signal with reduced incident intensity. To date, however, the XP2-SHG method has been implemented at only a single incident wavelength.[45,46] The present paper is devoted to applying the XP2-SHG method spectroscopically to embedded Si NCs of $\langle d_{NC} \rangle = 3$ and 5 nm, enabling detailed comparison with results from conventional spectroscopies, and insight into the relative importance of interfacial and bulk contributions. An SHG study of Si NCs of much larger $\langle d_{NC} \rangle > 50$ nm was recently reported.[47]

The paper is organized as follows: Section II describes, first, Si NC sample preparation and nonoptical characterization, and second, conventional optical spectroscopy studies: PL, SE, and Raman backscatter. Section III presents the XP2-SHG methodology, results, and analysis. Section IV discusses the combined optical spectroscopic results and uses the comparison to argue for a dominant NC/SiO$_2$ interfacial contribution to the XP2-SHG signal. Section V summarizes the main results and conclusions.

II. SAMPLES AND CONVENTIONAL SPECTROSCOPIC CHARACTERIZATION

In this section we report results of our conventional spectroscopic characterization of embedded Si NCs. Although many of these measurements are similar to measurements reported previously by others, we report them for the following reasons: (1) to provide a point of contact with previous results, and to show how our samples resemble, and differ from, those used by others; (2) to provide a comparison with the results of SHG spectroscopy; and (3) to provide linear optical constants required for quantitative analysis of SHG data. Specifically, the linear dielectric function extracted by SE enters Fresnel factors used in analysis of SHG data. In addition, our results include photoluminescence excitation (PLE) spectra of embedded Si NCs (Sec. II B), SE of as-implanted samples, and identification by SE of a resonance intermediate in energy between the E_1 and E_2 critical points (CPs) (Sec. II C).

A. Sample preparation

Samples were prepared by multienergy implantation of Si ions into bulk fused silica (Corning 7940 glass) substrates or into 1.7-μm-thick thermal oxide films grown on Si(100) wafers.[5,44,45] Si ions of six energies ranging from 35 to 500 keV were implanted to achieve a nearly uniform Si density over the implant depth of about 1 μm. Implanted samples were subsequently annealed at 1100 °C for 1 h in an atmosphere of either pure Ar or Ar/H$_2$ mixture to precipitate NC formation. NC samples with two different average NC diameters, $\langle d_{NC} \rangle = 3$ and 5 nm, were prepared from substrates dosed with excess Si densities of 0.5 and 1×10^{22} cm^{-3}, respectively. Cross-sectional transmission electron microscopy confirmed that spherical NCs with approximately 30% size fluctuation formed in the implant region (see, e.g., Fig. 1 of Ref. 5). These results imply that NCs form with density $\rho_{NC} = 7$ and 3×10^{18} cm^{-3} and occupy volume fraction 0.1 and 0.2, respectively, for 3 and 5 nm samples. One as-implanted sample dosed with 0.5×10^{22} cm^{-3} excess Si atoms was left unannealed. For all samples, an unimplanted rim was left in the outer 1 mm margin of the substrate, from which control spectra of the unimplanted glass substrate were measured. The Ar-annealed sample with 5 nm NCs was not of sufficient optical quality to yield reliable optical spectra. Thus for 5 nm NCs we report results only for the Ar/H$_2$ annealed sample.

B. Photoluminescence

Two types of PL spectra were measured: (1) spectroscopy of PL emission excited by a fixed wavelength ($\lambda = 488$ nm) Ar$^+$ laser and spectrally analyzed by a spectrometer equipped with a liquid-nitrogen-cooled charge-coupled device (CCD) and (2) PL excitation (PLE) excited by monochromatized, order-filtered light of a xenon arc lamp tuned over wavelength range $620 > \lambda > 248$ nm (photon energy range $2.0 < \hbar\omega < 5.0$ eV) and detected by a photomultiplier tube at a fixed wavelength at the peak of the PL emission spectrum. PLE signals were normalized to incident intensity.

The PL emission spectra in Fig. 1(a) show much stronger PL intensity from samples annealed in the presence of hydrogen, compared to those annealed in an inert atmosphere. This suggests the active role of the NC/SiO$_2$ interfaces in the PL process. H$_2$ saturates dangling bonds at these interfaces, thereby suppressing nonradiative decay mediated by these defects. Barely detectable PL peaked around 1.91 eV was observed (not shown) from the as-implanted sample and
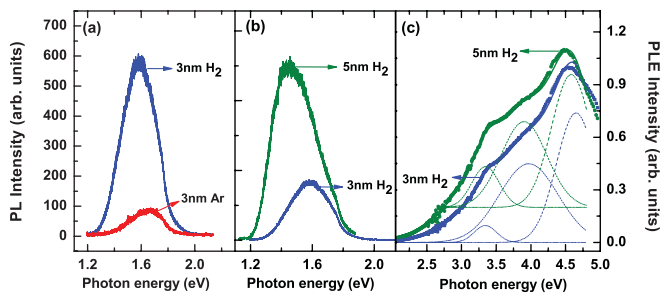
FIG. 1. (Color online) PL and PLE spectra of Si NCs embedded in SiO_2, normalized to intensity of excitation beam: (a) PL intensity of 3 nm samples annealed in Ar and Ar/H_2 mixture; (b) PL intensity from 3 and 5 nm NCs annealed in Ar/H_2 mixture; (c) PLE intensity from 3 and 5 nm NCs annealed in Ar/H_2. Data in (b) and (c) have been normalized to a common NC density ρ_{NC} by multiplying the 5 nm data by the ratio $\rho_{NC}^{(3\,nm)}/\rho_{NC}^{(5\,nm)}$. Solid curves in (c): fits of three-resonance model to the PLE data. Dotted curves: PLE intensities calculated from fit parameters for each individual resonance; the curves for the 5 nm data have been displaced upward to avoid crowding. Resonance energies, widths, and relative strengths obtained from the fit are given in Table I.

is attributed to defects introduced into the matrix during implantation that are repaired by annealing.[5] The normalized PL spectra in Fig. 1(b) illustrate the dependence of PL on NC size. The PL peak at 1.45 eV from the $\langle d_{NC} \rangle = 5$ nm sample blue shifts to 1.59 eV for the 3 nm sample, both annealed in Ar/H_2 mixture [Fig. 1(b)]. The PL emission spectra shown in Figs. 1(a) and 1(b) are consistent with previous PL spectra for similarly prepared samples.[5,13]

The normalized PLE spectra [Fig. 1(c)] show two distinct peaks around the bulk c-Si E_1 and E_2 critical points (3.37 and 4.27 eV, respectively), clear evidence that bulk c-Si structure prevails in these NCs and that the optical absorption that stimulates PL takes place in the c-Si region. A third strong feature can also be seen between these two peaks. To extract the energies, widths, and relative oscillator strengths of the resonant transitions contributing to absorption, we fit the PLE intensity to a superposition of three Gaussian resonances:

$$I(\omega) \propto \sum_{k=1}^{3} |f_k|^2 \exp\left[-2(\omega - \omega_k)^2/\gamma_k^2\right], \qquad (1)$$

with the resonance amplitudes f_k, frequencies ω_k, and widths γ_k being fit parameters. Gaussian line shapes provided a better fit than Lorentzians, and indicate the importance of inhomogeneous broadening. The solid curves in Fig. 1(c) show the fit to the data. The extracted parameters are listed in Table I, and calculated PLE intensities corresponding to the contributions of each individual oscillator are shown as dotted curves in Fig. 1(c). Three results of the fit are noteworthy. First, compared to the absorption spectrum of bulk c-Si, the E_1 peak of the NC PLE spectra is suppressed relative to the E_2 peak. Second, the fitted resonant energies corresponding to E_1 [$\hbar\omega_1 = 3.34 \pm 0.02$ (3 nm) and 3.35 ± 0.03 eV (5 nm)] remain almost unshifted, while E_2 [$\hbar\omega_3 = 4.65 \pm 0.03$ (3 nm) and 4.58 ± 0.04 eV (5 nm)] are blue shifted by 0.38 and 0.31 eV for 3 and 5 nm NCs from their bulk c-Si values. Third, the strong intermediate feature occurs around $\hbar\omega_2 = 3.90$ eV [$\hbar\omega_2 = 3.97 \pm 0.10$ (3 nm) and 3.90 ± 0.03 eV (5 nm)]. These findings will be discussed further, and compared to other spectroscopic measurements, in Sec. IV. PLE spectral structures similar to those shown in Fig. 1(c) were seen in porous silicon.[48,49]

C. Spectroscopic ellipsometry

Spectroscopic ellipsometry was used to confirm the thickness of the ~1-μm-thick Si NC-implanted layer, and to determine the dielectric function of the embedded Si NCs. Data was collected with a J.A. Woollam M2000 spectroscopic ellipsometer over the wavelength range $1000 > \lambda > 230$ nm (photon energy $1.24 < \hbar\omega < 5.4$ eV) in steps of 5 nm at $70°$ angle of incidence with the sample at room temperature. To avoid scattering from the back surfaces of samples with transparent silica substrates, SE data were collected on samples with silicon substrates. A four-phase model (Si/SiO_2/NC-embedded SiO_2/surface roughness) of the optical properties of the whole sample was developed. In the Si NCs/SiO_2 composite layer, a Bruggeman effective medium approximation was used to isolate the contribution from NCs.

To fit the measured ellipsometric angles Ψ and Δ satisfactorily throughout the spectral range, we found that a physical model of the dielectric function of the NCs was required, rather than the empirical superposition of Gaussians given by Eq. (1). There were two reasons for this. First, the SE data extended

TABLE I. Parameters of three oscillators between 3 and 5 eV determined by PLE, SE, and SHG. Oscillator amplitudes are expressed as a fraction of the amplitude of the E_2 resonance of the 5 nm NC sample for each spectroscopy. Numbers in parentheses are uncertainties.

Sample	Oscillator parameter	E_1			Intermediate peak			E_2		
		PLE	SE	SHG	PLE	SE	SHG	PLE	SE	SHG
3 nm	$\hbar\omega_k$ (eV)	3.33	3.3(0.4)	3.5(1)	4.0(0.1)	4.0 (0.3)	3.9	4.65	4.4 (0.1)	4.9
(Ar)	FWHM (eV)	0.3(0.1)	0.7(0.4)	0.5	0.8(0.3)	0.77	0.96	0.55	0.37	0.3
	amplitude	0.1	0.08(0.04)	0.08(0.04)	0.3	0.41	1.05	0.48	0.71	0.5
3 nm	$\hbar\omega_k$ (eV)	3.34	3.3(0.4)	3.5(0.8)	4.0(0.1)	4.0(0.2)	3.84	4.65	4.4(0.1)	4.9
(Ar/H_2)	FWHM (eV)	0.4(0.1)	0.7(0.4)	0.46	0.8(0.3)	0.81	0.58	0.55	0.35	0.3
	amplitude	0.15(0.1)	0.07(0.03)	0.1(0.05)	0.35	0.41	0.64	0.44	0.73	0.54
5 nm	$\hbar\omega_k$ (eV)	3.35	3.35(0.2)	3.4	3.9	3.9(0.5)	3.73	4.58	4.35(0.4)	4.8
(Ar/H_2)	FWHM (eV)	0.46	0.45(0.1)	0.3	0.6(0.2)	0.65	0.34	0.5	0.37	0.28
	amplitude	0.55	0.17	0.88	0.35	0.39	0.79	1.0	1.0	1.0

to somewhat higher photon energies than the PLE data. As a result, we found that a fourth oscillator at $\hbar\omega_4 \approx 5.9$ eV was essential to fit Ψ and Δ in the highly absorbing region $5.0 < \hbar\omega < 5.4$ eV. Secondly, for SE both amplitude and phase of reflected light must be fitted simultaneously, more tightly constraining the model than PLE intensity data. In particular, line shapes required a more accurate representation to account for both their natural widths and inhomogeneous broadening caused by NC size distribution. We therefore employed four Gauss-Lorentz oscillators to model the dielectric function of the NCs. The dielectric function in the Gauss-Lorentz oscillator model is given by

$$\varepsilon_{\mathrm{LG}}(E) = \varepsilon_\infty + \sum_{n=1}^{4} i A_n \left[\int_0^\infty e^{i[E - E_n + i\gamma_n(s)]s} \, ds \right.$$
$$\left. - \int_0^\infty e^{i[E + E_n + i\gamma_n(s)]s} \, ds \right] \bigg/ \int_0^\infty e^{-s\gamma_n(s)} \, ds, \quad (2)$$

where ε_∞ is the dielectric constant at large photon energies (set to 1 for fitting), and A_n is the oscillator strength, E_n is the center energy, and $\gamma_n(s)$ is the broadening parameter of the nth oscillator. The broadening parameter is a frequency-dependent function instead of a constant: $\gamma_n(s) = \Gamma_n + 2\sigma_n^2 s$, where Γ_n and σ_n are the parameters defining the contribution of Lorentzian and Gaussian broadening, respectively, to the total broadening. The pure Lorentz oscillator model is recovered in the limit $\sigma_n \to 0$, while the pure Gaussian oscillator model is recovered for $\Gamma_n \to 0$. This significantly improved fits to the measured Ψ and Δ compared to fits based on either pure Lorentzian or pure Gaussian oscillators; the former had been used in some previous SE studies of embedded Si NCs.[23] The NCs were assumed homogeneous; no internal components were distinguished in the model. A surface-roughness layer several nanometers thick was introduced to take into account damage on the surface of the samples induced by ion implantation. The NC oscillator parameters, the thickness of each layer, and the NC volume fraction were treated as fitting parameters. The fitted implant layer thicknesses (as-implanted: 935 ± 4 nm; 3 nm NCs annealed in Ar and Ar/H$_2$: 954 ± 4 nm and 954 ± 4 nm, respectively; 5 nm NCs annealed in Ar/H$_2$: 979 ± 7 nm) and the NC volume fraction (as-implanted: 0.10; 3 nm NCs annealed in Ar and Ar/H$_2$: both 0.10; 5 nm NCs annealed in Ar/H$_2$: 0.194) were consistent with values determined independently, as described in Sec. II A. The fit yielded good agreement between experimental and calculated Ψ and Δ spectra, as shown by the Ψ,Δ plot in Fig. 2.

Figure 3 shows the extracted dielectric functions $\varepsilon_1(\omega) + i\varepsilon_2(\omega)$ of as-implanted [(a), ε_1 and (e), ε_2] and Si NC [(b)–(d), ε_1 and (f)–(h), ε_2] samples. The dielectric functions of bulk a-Si [panels (a) and (e), Ref. 50] and c-Si (remaining panels, Ref. 51) are shown for comparison. For the as-implanted sample, an excellent fit to the measured Ψ and Δ was obtained by modeling the dielectric function of the implanted excess Si using only two Gauss-Lorentz oscillators at 3.95 and 4.8 eV, as shown in the plot of ε_2 in Fig. 3(e). The 3.95 eV peak is similar in shape to the 3.6 eV peak in the ε_2 of a-Si [dashed curve in Fig. 3(e)]. The similarly shaped spectrum and blueshift suggest that the as-implanted sample contains extremely small nanoparticles of a-Si. The Raman
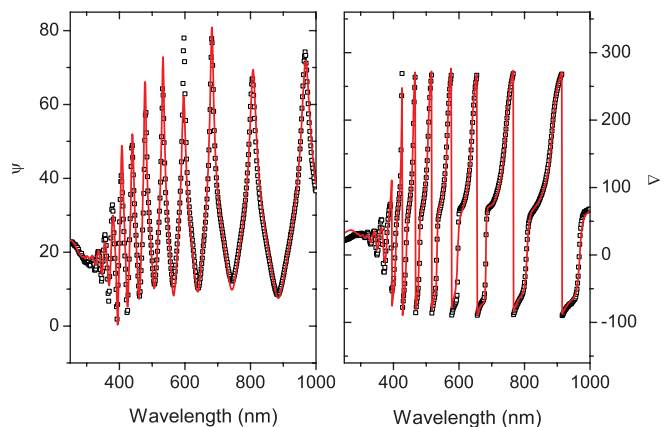

FIG. 2. (Color online) Measured Ψ (left) and Δ (right) for 5 nm NC sample annealed in Ar/H$_2$, compared to fits (red curves) based on Gauss-Lorentz oscillator model of the dielectric function of the NC layer.

spectrum of the as-implanted sample, discussed in the next section, also supports this conclusion. The higher-energy ε_2 component may correspond to a second feature observed in the Raman spectrum that we tentatively attribute to stressed Si-Si bonds at the interfaces of the a-Si nanoinclusions. For the annealed NC samples, ε_2 shows a dominant peak at 4.43 eV [3 nm NCs, Figs. 3(f) and 3(g)] or 4.35 eV [5 nm NCs, Fig. 3(h)], close to the energy of the dominant peak of the PLE spectra [Fig. 1(c)]. This peak is consistent with an E_2 CP transition. There are also two lower-energy shoulders at $\sim$4.0 and $\sim$3.3 eV with energies close to corresponding features of the PLE spectra of these samples [Fig. 1(c)]. Both shoulders are clearly discernible for the 5 nm sample [Fig. 3(h)]. For the 3 nm samples, the weak $\sim$3.3 eV feature is discernible with only an extended low-energy tail of the $\sim$4.0 eV shoulder. In both cases, the $\sim$3.3 eV feature is consistent with an E_1 CP transition. The appearance of CP transitions further evidences crystallization of the NCs. The individual contributions from the three Gauss-Lorentz oscillators corresponding to these three features, and from a fourth oscillator at higher energy [5.8 eV, panel 3(f); 5.9 eV, panel 3(g); 5.8 eV, panel 3(h)], are shown by thin solid curves in panels 3(f)–3(h). The extracted parameters of the three oscillators below 5 eV are listed in Table I.

Several features of the results in Fig. 3 are noteworthy. First, the overall shapes of the $\varepsilon_2(\omega)$ curves for the annealed NC samples [Figs. 3(f)– 3(h)] closely resemble the corresponding PLE spectra [Fig. 1(c)], consistent with their common physical connection to linear optical absorption. The positions of the three peaks below 5 eV are consistent between PLE and SE within the error estimates given in Table I, although the uncertainty in $\varepsilon_2(\omega)$ peak positions was too large to confirm unambiguously the size-dependent blueshifts discussed in Sec. II B. One difference is that in $\varepsilon_2(\omega)$, the E_1 peak is more strongly suppressed relative to E_2 and to the intermediate $\sim$4.0 eV peak than in the PLE spectra. For 3 nm NC samples [Figs. 3(f) and 3(g)] it is barely discernible. In both SE and PLE spectra, the E_1/E_2 amplitude ratio is smaller than in $\varepsilon_2(\omega)$ of bulk c-Si [Figs. 3(f)–3(h), dashed curves]. A similar E_1 suppression was also observed in previous SE studies of Si
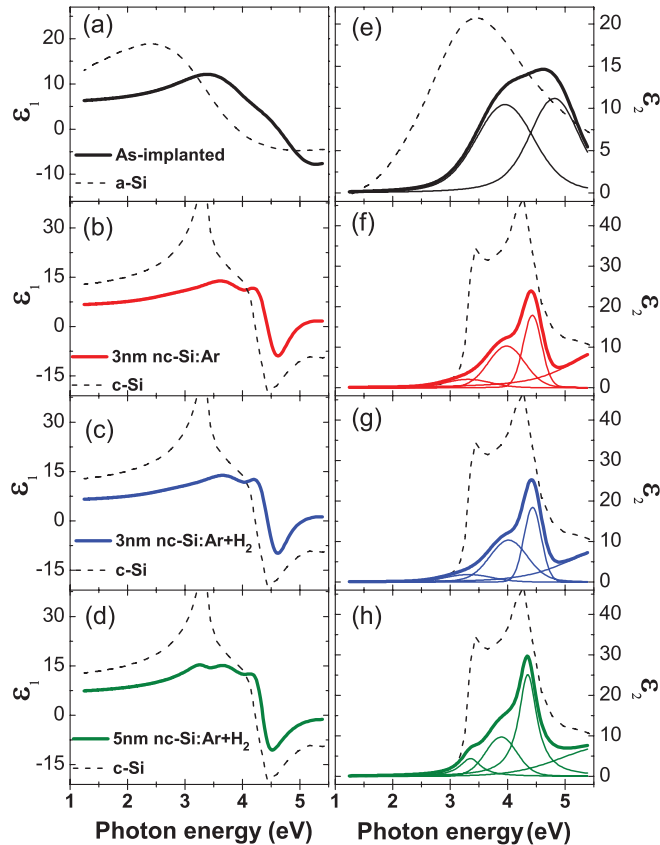
FIG. 3. (Color online) Real [(a)–(d)] and imaginary [(e)–(h)] parts of the dielectric functions $\varepsilon_1 + i\varepsilon_2$ (bold solid curves) extracted from SE measurement of various Si implants: as-implanted [(a) and (e)], bold solid black curves]; 3 nm NCs annealed in Ar [(b) and (f), bold solid red curves]; 3 nm NCs annealed in Ar/H$_2$ mixture [(c) and (g), bold solid blue curves]; 5 nm NCs annealed in Ar/H$_2$ mixture [(d) and (h), bold solid olive curves]. Dielectric functions of bulk a-Si [thin black curves in (a) and (e), Ref. 50] and c-Si [thin black curves in (b)–(d) and (f)–(h), Ref. 51] are shown for comparison. Thin solid curves in each panel show the contributions from each oscillator used to model the dielectric function of the implanted Si region.
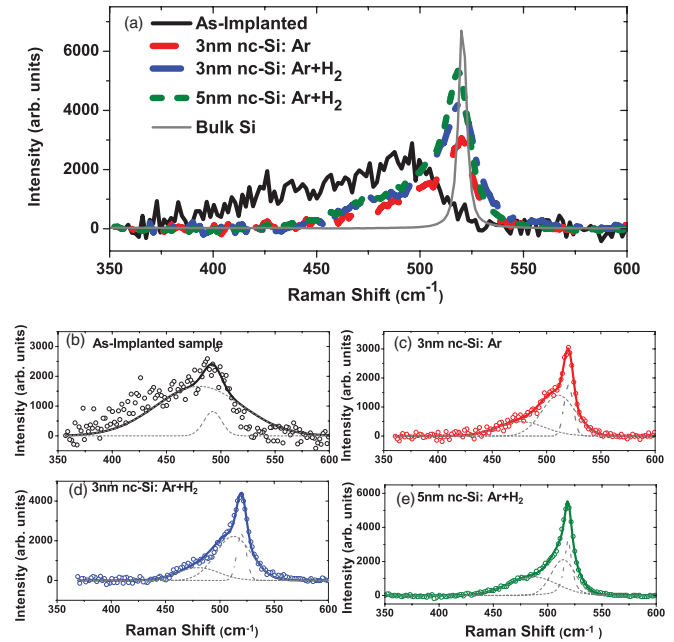

FIG. 4. (Color online) (a) Raman backscatter spectra of as-implanted sample (black solid), 3 nm NCs annealed in pure Ar (red dashed), 3 nm NCs annealed in Ar/H$_2$ mixture (blue dash-dotted), 5 NCs nm annealed in Ar/H$_2$ mixture (olive short-dashed), and a reference bulk c-Si sample (gray thin curve). In the remaining panels, the Raman spectrum of each sample is decomposed into Lorentz oscillator contributions: (b) as-implanted, (c) 3 nm NCs annealed in pure Ar, (d) 3 nm NCs annealed in Ar/H$_2$ mixture, and (e) 5 nm NCs annealed in Ar/H$_2$ mixture.

NCs embedded in SiO$_2$,[25] and in *ab initio* calculations of the optical properties of Si NCs in SiO$_2$.[52,53] Secondly, for 3 nm NCs, the extracted $\varepsilon_1(\omega)$ and $\varepsilon_2(\omega)$ are indistinguishable for samples annealed in Ar/H$_2$ mixture and pure Ar [see curves in Figs. 3(b), 3(c), 3(f), and 3(g)]. This indicates that the dielectric function, unlike the PL shown in Fig. 1(a), reflects properties of the c-Si interior that are unaffected by interfacial H passivation. Thirdly, the amplitudes of ε_1 and ε_2 in the E_1-E_2 resonance region, which in Fig. 3 are normalized to an equivalent amount of Si material, are much smaller for NCs than for bulk Si, and slightly smaller for 3 nm than for 5 nm NCs. A similar reduction in the dielectric function has been observed in previous SE studies of Si NCs.[23–25]

D. Raman spectroscopy

Raman spectroscopy elucidates the microstructure of the Si NCs.[31] Raman backscatter of a 514.5 nm argon laser beam focused onto the sample with a 50× microscope objective was collected with a Renishaw inVia microscope. Figure 4(a) compares Raman spectra from the as-implanted sample (black solid curve), Si NC samples annealed in Ar with $\langle d_{NC} \rangle = 3$ nm (red dashed curve), and in Ar/H$_2$ mixture with $\langle d_{NC} \rangle = 3$ nm (blue dash-dotted curve) and 5 nm (olive short-dashed curve), and a reference bulk c-Si sample (gray thin solid curve). The c-Si sample yields a single sharp Raman peak at 520 cm^{-1}; the Raman spectra of the other samples are broadened to varying extents toward lower frequencies.

To analyze the content of the latter spectra, Figs. 4(b)–4(d) deconvolve and fit them using Lorentzian functions centered at frequencies that were treated as fitting parameters.[27] The dominant component of the Raman spectrum of the as-implanted sample is a broad asymmetric peak centered around 480 cm^{-1} [see Fig. 4(b)], corresponding to Si-Si bonds in a-Si.[31] This suggests that excess Si in the as-implanted sample is primarily in a-Si form, as Kachurin *et al.*[31] concluded in a previous Raman spectroscopy study. Kachurin *et al.*[31] found that when the average distance between excess Si atoms approaches ~1 nm, as is the case for our sample, small a-Si clusters form as a result of density fluctuations of the excess Si. This picture of small amorphous Si nanoclusters is consistent with our observation of a strongly blue-shifted a-Si-like ε_2 peak from SE analysis of this sample [see Sec. II C and Fig. 3(e)]. The Lorentzian oscillator fit also reveals a weaker peak around 490 cm^{-1}. This feature may correspond to the 4.8 eV peak in ε_2 discussed in the previous section, and

may originate from stressed Si-Si bonds at the interfaces of amorphous nanoclusters.

For annealed NC samples, the deconvolved Raman spectra show a sharp peak around 520 cm^{-1}, characteristic of c-Si, that is much stronger for $\langle d_{NC} \rangle = 5$ nm than for 3 nm. In addition, there is a broad asymmetric shoulder on the lower-energy side, extending through the 480 cm^{-1} resonance characteristic of a-Si. The spectra of the 3 and 5 nm NCs were fitted to three Lorentzian functions associated with three classes of Si structures: a-Si with peak around 480 cm^{-1}, c-Si with peak at 520 cm^{-1}, and a third peak at $\sim$510 cm^{-1} that we attribute to the transitional grain boundary between the NCs and the silica matrix. The 480 cm^{-1} component clearly indicates the presence of residual a-Si content in the annealed samples, despite crystallization signified by the 520 cm^{-1} component. The 510 cm^{-1} peak evidently evolved from the 490 cm^{-1} peak observed in the as-implanted sample, and is attributed analogously to scattering from Si-Si bonds at NC/SiO$_2$ interfaces. Relative to the 480 and 520 cm^{-1} components, this contribution is weighted more heavily for the 3 nm than for the 5 nm sample. These results are consistent with *ab initio* calculations by Daldosso *et al.*[15] showing that Si NCs of a few nanometers diameter embedded in amorphous oxide develop a c-Si core surrounded by a transitional shell composed of a-Si and substoichiometric oxide. Moreover, molecular dynamics simulations of annealed samples[16] show that smaller NCs have larger fractional a-Si content, and become completely amorphous for $\langle d_{NC} \rangle$ less than $\sim$2 nm, consistent with our Raman and SE results for as-implanted samples.

Close inspection of the Lorentz fits shows that the c-Si peak for 5 nm samples is at 518.9 cm^{-1}, slightly *smaller* than 520.3 cm^{-1} for 3 nm samples. This trend contradicts quantum confinement theory, which predicts a shift to smaller wave numbers with decreasing particle size, as observed by several groups.[29–31] On the other hand, Hernandez *et al.*[28] reported an anomalous shift similar to ours in Si NCs embedded in SiO$_2$ created by annealing Si-rich SiO$_x$ films. That result was attributed to hydrostatic stress, which strengthens with decreasing NC sizes, overcoming the quantum confinement effect and upshifting the peak.[28]

III. SECOND-HARMONIC GENERATION SPECTROSCOPY

In this section, we report our spectroscopic XP2-SHG results for 3 and 5 nm average diameter Si NCs embedded in SiO$_2$, extending previous single-beam[44] or single-wavelength[45] studies. Preliminary XP2-SHG data for only 3 nm Si NC samples was published in 2008.[54] However, the extracted nonlinear coefficients there were only approximate because SE data was not available at that time to determine Fresnel coefficients needed for quantitative XP2-SHG spectral analysis. Here we extract nonlinear coefficients making use of the measured linear dielectric function. Results for 5 nm NCs and as-implanted sample, and XP2-SFG (sum-frequency generation) spectra, are reported.

A. Quadrupolar SHG from nanoparticles and glass matrix

In centrosymmetric media, electric dipolar SHG vanishes. In media that are also isotropic and homogeneous, such as the amorphous SiO$_2$ matrix, the leading radiating part of the nonlinear polarization is quadrupolar and can be written in the form[55]

$$\vec{P}_Q^{(2)}(2\omega) = \Gamma[\vec{E}(\omega) \cdot \nabla]\vec{E}(\omega), \tag{3}$$

where Γ is a material constant. Centrosymmetry is broken at surfaces/interfaces of centrosymmetric materials because of structural and chemical discontinuity. For planar surfaces/interfaces, electric dipolar SHG then becomes allowed, making SHG a noninvasive probe of planar interfaces of centrosymmetric materials. But for spherical nanoparticles, locally broken centrosymmetry at NC interfaces is recovered globally. A nonzero total radiating SH polarization arises only because of retardation[41] and/or incident field inhomogeneity[42,43] over the dimensions of the nanoparticle. Spatial averaging of the local interface electric dipolar contribution plus the quadrupolar contribution from the bulk interiors of the nanoparticles yields a macroscopic nanocomposite SH polarization of the same form as Eq. (3),[43]

$$\vec{P}_{NC}^{(2)}(2\omega) = \rho_{NC}\left(\gamma^e - \gamma^m - \frac{\gamma^q}{6}\right)[\vec{E}(\omega) \cdot \nabla]\vec{E}(\omega), \tag{4}$$

where the hyperpolarizabilities γ^e, γ^m, and γ^q are functions of the multipolar bulk susceptibilities and dipolar interface susceptibilities of the material comprising the nanoparticles, and ρ_{NC} is the nanoparticle density, assumed uniform. Additional contributions arise when nanoparticle density gradients are present.[43]

Thus both embedded NCs and the amorphous SiO$_2$ matrix contribute to SHG. Three parameters must therefore be determined at each wavelength to analyze SHG data from the nanocomposite: the amplitudes $|\Gamma_{NC}|$ and Γ_g of the SH polarizations $P_{NC}^{(2)}(2\omega)$ and $P_g^{(2)}(2\omega)$, respectively, from the NC-embedded layers and glass substrate, and the phase difference Φ between them. We thus parametrize the SH polarizations as follows:

$$\vec{P}_{NC}^{(2)}(2\omega) = |\Gamma_{NC}|e^{i\Phi}[\vec{E}(\omega) \cdot \nabla]\vec{E}(\omega), \tag{5}$$

$$\vec{P}_g^{(2)}(2\omega) = \Gamma_g[\vec{E}(\omega) \cdot \nabla]\vec{E}(\omega), \tag{6}$$

where Γ_g is assumed to be real. In fitting data and presentation of results, Γ_{NC} will represent the composite SH response of the entire 1-μm-thick NC-implanted layer (both glass and Si NCs), while Γ_g will represent the SH response of the 1-mm-thick underlying SiO$_2$ substrate.

B. XP2-SHG procedure

A two-beam geometry was used to enhance quadrupolar SHG efficiency greatly compared to conventional single-beam SHG.[45] The enhancement occurs because the interaction of two orthogonally polarized beams intersecting at oblique angle α inside the sample induces wavelength-scale, forward-radiating inhomogeneities in SH polarization fields of the form of Eqs. (3)–(6) that are absent for single-beam
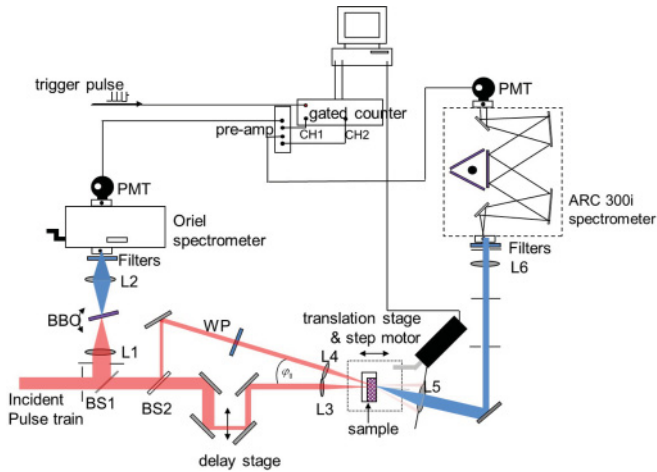
FIG. 5. (Color online) XP2-SHG setup. Beam splitter BS1 splits off a reference pulse train from the incident tunable fundamental beam. BS2 splits the remaining beam into two pulse trains. One impinges normally, one obliquely onto the sample with pulses overlapped spatially and temporally after focusing to common spot radius 70 μm by lenses L3 and L4. Half-wave plate WP rotates the polarization of the obliquely incident beam by 90°. SHG propagating along the bisector of the two incident beams is detected by a photomultiplier tube (PMT) in photon-counting mode.

FIG. 6. (Color online) Representative experimental results (data points) and model fits (curves) of XP2-SHG z-scan measurements for incident wavelengths 550 (left) and 710 nm (right) for 3 (upper) and 5 (bottom) nm NC samples annealed in Ar/H$_2$ mixture. Olive (diamond data points, solid curve): z scan with unimplanted glass; red (filled square data points, dash-dotted curve): z scan with NCs at exit side of sample; blue (filled circles, dashed curve): z scan with NCs at entrance side of sample). SH intensity from unimplanted glass (olive) is approximately the same for all wavelengths and samples.

excitation.[45] Figure 5 shows the XP2-SHG experimental setup. A home-built noncollinear optical parametric amplifier (NOPA)[56] provided incident ∼250 fs, 3–12 μJ pulses at 1 kHz repetition rate with photon energy $\hbar\omega$ tunable over the range 1.6 ⩽ $\hbar\omega$ ⩽ 2.4 eV. The second-harmonic photon energy $\hbar\omega_{SH} = 2\hbar\omega$ thus tuned over the range 3.2 ⩽ $\hbar\omega_{SH}$ ⩽ 4.8 eV. An angle-tuned β-BaB$_2$O$_4$ (BBO) crystal pumped by 100 μJ, 400 nm pulses derived from frequency doubling the output of a Ti:sapphire femtosecond laser-amplifier system (Spectra-Physics, Inc. Model Spitfire) served as the parametric amplification medium. A chirped white-light continuum generated in sapphire by a 1% split-off portion of the 800 nm fundamental pulses from the Ti:sapphire system provided the seed pulse for parametric amplification. 800 nm pulses directly from the Ti:sapphire system were used to obtain a single additional XP2-SHG data point at $\hbar\omega = 1.55$ eV ($\hbar\omega_{SH} = 3.1$ eV). A 50/50 beam splitter (BS2 in Fig. 5) divided the incoming pulse train into two equivalent beams. One beam impinged at normal incidence onto the sample (hereafter the z direction), the other at an oblique angle (typically ∼20°) with its polarization rotated 90° with respect to the first beam by a half-wave plate. Pulses in each beam were focused to spot radius 70 μm and spatially-temporally overlapped in the sample. The SHG signal, propagating in the bisector direction, was collimated, spectrally filtered by a monochromator, and detected by a photomultiplier tube in gated photon-counting mode. An additional small part of the incoming laser pulse train was sent to a BBO crystal to generate a reference SHG signal that monitored drifts in pulse energy and pulse duration during spectral tuning. To distinguish one-photon and two-photon resonances in the XP2-SHG spectrum, a portion of the measurements was repeated using XP2-SFG. In this case, a 10%-split-off portion of the 800 nm Ti:sapphire pulse train provided one of the intersecting beams, while the
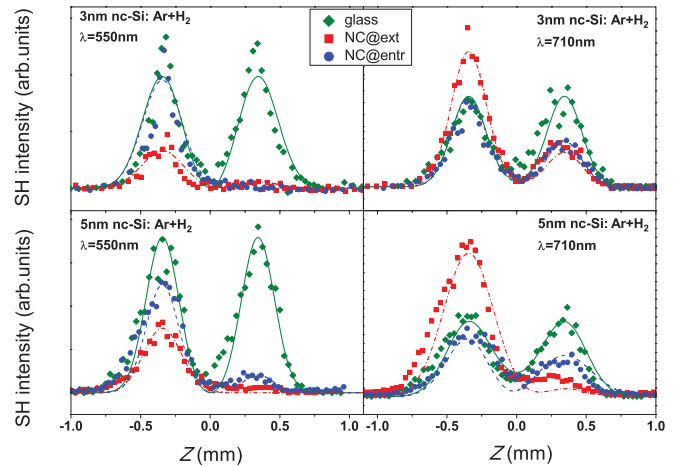
tunable NOPA pulse train provided the other. Thus the SF photon energy $\hbar\omega_{SF} = 1.55 + \hbar\omega$ tuned over the range 3.15 ⩽ $\hbar\omega_{SF}$ ⩽ 3.95 eV. To reveal resonant structure just beyond the upper end of the XP2-SHG spectral range, XP2-SFG using the tunable NOPA pulse train and the frequency-doubled (400 nm) Ti:sapphire pulse train was conducted. This extended the upper end of the spectral range from 4.8 to 5.1 eV.

Both the embedded NCs and the silica substrate produce XP2-SHG signals. In order to separate these contributions, three independent measurements were performed at each wavelength in order to determine the three unknowns $|\Gamma_{NC}|$, Γ_g, and Φ in Eqs. (5) and (6). Each measurement consisted of a z scan—i.e., a translational scan of the sample along the z direction through the fixed-beam overlap region. In one measurement, the pure glass sample edge with no NCs was z scanned while the XP2-SHG signal was recorded as a function of sample position. In the other two measurements, the NC-embedded part of the sample z scanned through the beam overlap region, once with the NC layer at the entrance face of the sample and once with the NC layer at the exit face. Figure 6 shows representative results for incident wavelengths 550 (left) and 710 nm (right) for 3 (upper) and 5 (bottom) nm NC samples annealed in Ar/H$_2$ mixture. In all cases, two peaks in the SHG intensity vs sample position were observed, namely, when the center of the beam overlap region coincided with each of the two surfaces of the sample. The peaks come *not* from interface SHG but from relaxation of phase mismatch when boundaries of the sample fall within the two-beam overlap region.[46] In the pure glass z scan (olive, diamond data points, solid curves in Fig. 6) these peaks were identical in intensity because of the symmetry of the front and rear surfaces of pure glass. For the other z scans, these two peaks were asymmetric because of interference between the SH fields from the NCs and the glass matrix. Absorption
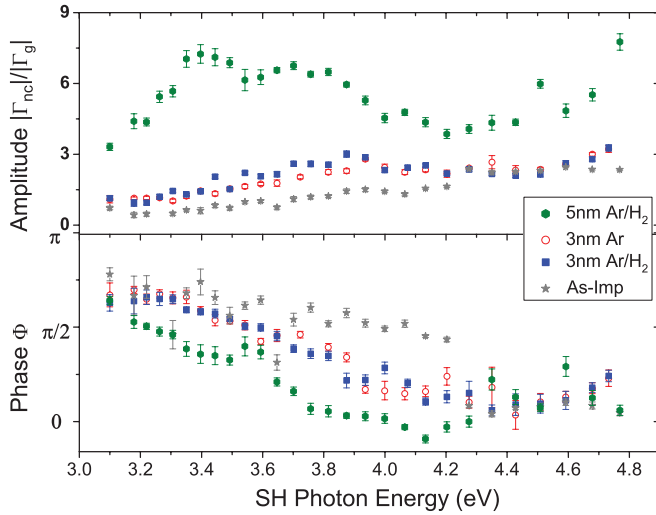
FIG. 7. (Color online) XP2-SHG spectral response of Si NC samples plotted vs second-harmonic photon energy $\hbar\omega_{SH}$. Upper panel: SH amplitudes (Γ_{NC} and $\Gamma_{as\text{-}imp}$) normalized to SH amplitude of glass matrix (Γ_g); lower panel: phase difference Φ between SH fields from NCs and glass. Gray (stars): as-implanted sample; blue (filled squares): 3 nm Si NCs annealed in Ar/H_2; red (open squares): 3 nm Si NCs annealed in Ar; olive (filled circles): 5 nm Si NCs annealed in Ar/H_2.

and phase delay of the fundamental and SH beams in the NC layer also affect the SH intensity profile. A phenomenological model that took these factors into account was then fitted to the measured z-dependent SH intensity profiles (see curves in Fig. 6), enabling deconvolution of the interfering SH fields and extraction of their normalized amplitude $|\Gamma_{NC}|/\Gamma_g$ and phase difference Φ. Very good fits were obtained throughout the spectral range. Additional details of the z-scan procedure, modeling, and fitting were described in Ref. 54.

C. XP2-SHG spectra of Si NCs

Figure 7 presents SHG spectra of 3 and 5 nm Si NC samples and the as-implanted sample. Normalized amplitudes Γ_{NC}/Γ_g ($\Gamma_{as\text{-}imp}/\Gamma_g$) (upper panel) and phase differences Φ (lower panel) of these samples are plotted vs second-harmonic photon energy $\hbar\omega_{SH}$. Since Γ_g is nearly featureless in the measured spectral range, all spectral features should come from embedded nanoparticles. For all annealed samples, Γ_{NC} significantly exceeds Γ_g throughout the measured spectral range. The corresponding $\Phi(\hbar\omega_{SH})$ decrease monotonically with increasing $\hbar\omega_{SH}$ throughout the region of elevated SH oscillator strength, with slope roughly proportional to the corresponding amplitude. These features are qualitatively consistent with a Kramers-Kronig relation between amplitudes and phases of the SHG responses, as discussed further below.

Apart from this common feature, the SHG spectra of the various samples differ markedly. The as-implanted layer exhibits the weakest SHG response [Fig. 7, gray stars, and Fig. 8(a)]. For $\hbar\omega_{SH} < 3.6$ eV, $\Gamma_{as\text{-}imp}$ is actually slightly *less* than Γ_g, then increases continuously up to $\sim 2\Gamma_g$ at the upper end of the $\hbar\omega_{SH}$ range. The weakness of the SH response compared to c-Si and the featureless monotonic increase in SH amplitude from $\hbar\omega_{SH}\sim 3$ eV to $\hbar\omega_{SH}\sim 4.5$ eV both
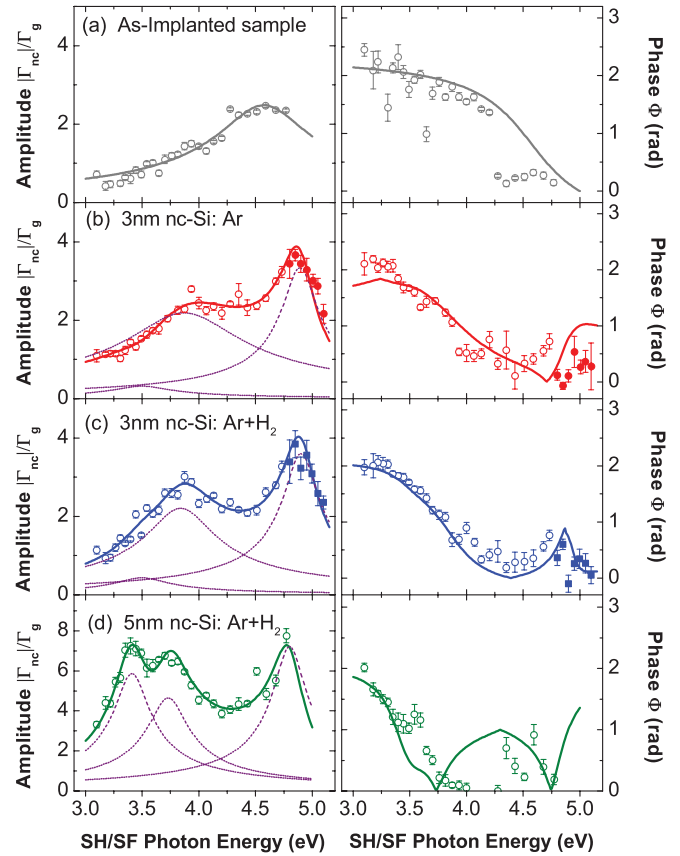

FIG. 8. (Color online) Combined XP2-SHG/SFG amplitude (left-hand panels) and phase (right-hand panels) spectra (data points and samples as in Fig. 7) and fits (solid curves) to a three-oscillator model of the SH polarization. Dashed curves in left-hand panels show the individual contributions of each oscillator. Data points acquired by XP2-SFG in the range $4.8 < \hbar\omega_{SF} < 5.1$ eV are denoted by filled red circles (b) and filled blue squares (c) for 3 nm NC samples annealed in Ar and Ar/H_2, respectively. All other data points were acquired by XP2-SHG.

resemble the SHG spectrum of bulk a-Si reported by Daum and co-workers (see Fig. 1 of Ref. 39). These features are also consistent with a-Si-like features in the SE and Raman spectra of the as-implanted samples reported in Secs. II C and II D, respectively.

The SHG spectra of 3 nm NCs annealed in pure Ar [Figs. 7 (red open circles) and 8(b)] and in Ar/H_2 [Figs. 7 (blue filled squares) and 8(c)] remain quite featureless, except for broad resonances in $|\Gamma_{NC}(\hbar\omega_{SH})|$ around 3.8 eV and at 4.8–4.9 eV [see Figs. 8(b) and 8(c), left-hand panels] that were not observed in $\Gamma_{as\text{-}imp}(\hbar\omega_{SH})$. The spectra of the two samples are very similar to each other, showing that SHG is insensitive to the nanointerfacial hydrogen termination of the latter sample. The 3.8 eV resonance is close in energy to the feature between E_1 and E_2 observed by PLE [see Fig. 1(c) and Table I] and SE [see Figs. 3(f), 3(g), and Table I] of these samples. It is also equal in energy to a prominent non-CP resonance observed in the SHG spectrum of planar Si(001)/SiO_2 interfaces by Daum and co-workers,[39] who attributed it to interfacial Si atoms without T_d lattice symmetry. Remarkably, however, no peak appears in the XP2-SHG spectrum at the energy

of the prominent E_2-like resonance observed in both PLE [4.65 ± 0.03 eV, see Fig. 1(c)] and ε_2 [4.4 ± 0.1 eV, see Figs. 3(f) and 3(g)] of these samples. Instead, the rising $|\Gamma_{NC}(\hbar\omega_{SH})|$ at the upper end of the $\hbar\omega_{SH}$ range suggests the presence of a peak at $\hbar\omega_{SH}\sim4.8$ eV, just beyond the upper limit of the XP2-SHG tuning range. The existence of this peak is confirmed by XP2-SFG (400 nm + NOPA) data for the 3 nm samples in the range $4.8 < \hbar\omega_{SF} < 5.1$ eV, plotted as filled red circles [Fig. 8(b)] and filled blue squares [Fig. 8(c)] in the combined XP2-SHG/SFG spectra presented in Fig. 8. In Sec. IV D we show that the E_2-like resonance can appear blue shifted in SHG compared to its position in SE. Thus we shall refer to this ~4.8 eV feature as an E_2-like resonance despite the apparent discrepancy in its resonant energy.

For the annealed 5 nm NC layer, $|\Gamma_{NC}/\Gamma_g|$ increases sharply at all wavelengths compared to the 3 nm NC layer [Figs. 7 (olive filled circles) and 8(d)]. Averaged over the entire spectral range, $|\Gamma_{NC}/\Gamma_g|$ is approximately four times stronger for the 5 nm NC layer than for the 3 nm NC layer. Normalizing to NC density [$\rho_{NC}^{(5\,nm)} = (3/7)\rho_{NC}^{(3\,nm)}$], we find that on spectral average $|\Gamma_{NC}^{(5\,nm)}/\Gamma_g| \approx 10|\Gamma_{NC}^{(3\,nm)}/\Gamma_g|$ per NC. Although strong, this NC-size dependence falls somewhat short of the ideal ratio $(5/3)^6 \approx 21$ predicted by a single-centrosymmetric-nanosphere theory of SHG.[41] A spectral feature emerges from the 5 nm NCs: a prominent resonance near the bulk c-Si E_1 CP transition energy at 3.4 eV [Figs. 7 (olive filled circles) and 8(d)]. This peak corresponds closely in energy to the low-energy shoulder (3.35 eV) observed in the PLE spectrum [Fig. 1(c)], and to the lowest-energy shoulder (3.35 ± 0.2 eV) observed in the ε_2 spectrum [Fig. 3(h)], of this sample. In addition, prominent resonances near 3.7 and 4.8 eV, very close in energy to the two SHG peaks observed from the 3 nm NC layer, appear with increased amplitude. The latter feature is again at significantly higher energy than the E_2-like peak (~4.4 eV), observed prominently in the linear PLE and ε_2 spectra. Strong absorption of the SFG signal prevented acquisition of extended XP2-SFG data in the range $4.8 < \hbar\omega_{SF} < 5.1$ eV for the 5 nm sample.

To extract resonant energies and widths and to relate amplitude and phase SHG spectra (upper and lower panels of Fig. 7 and left-hand and right-hand panels of Fig. 8) to each other quantitatively, we modeled Γ_{NC} as a coherent superposition of three resonances with excitonic line shapes,

$$\Gamma_{NC}(2\omega) \propto \sum_{k=1}^{3} \frac{f_k \exp(i\psi_k)}{2\omega - \omega_k + i\gamma_k}, \tag{7}$$

where f_k is the resonance amplitude, ψ_k is the resonance phase, ω_k is the resonance energy, and γ_k is the damping parameter. Similar empirical models have been used previously to analyze resonant structure of SHG spectra.[39,57] The parameters f_k, ψ_k, ω_k, and γ_k were varied to achieve the best fit to the amplitude spectra $\Gamma_{NC}(\hbar\omega_{SH})/\Gamma_g$. The phase spectra $\Phi(\hbar\omega_{SH})$ were then reconstructed from the fitting result and compared with experimental results to check Kramers-Kronig consistency of the SHG spectra. Lorentzian resonances instead of Gaussian (as for PLE) were used here considering the coherent interference of different resonances with complete amplitude and phase information.

The solid curves in the left-hand panels of Fig. 8 show the fits to the SHG amplitude spectra for each sample. The dashed curves in the same panels show the individual contributions from each resonance. Table I lists the fitted resonant energies $\hbar\omega_k$, full width at half maximum (FWHM), and relative amplitudes f_k for the annealed samples. For the as-implanted sample, the fit yielded a single dominant broad resonance around 4.57 eV [Fig. 8(a), left-hand panel]. This resonance energy is consistent with the average energy (~4.5 eV) of the feature in the linear ε_2 of this sample [see Fig. 3(e)], which was modeled as a superposition of resonances at 3.95 and 4.8 eV and indicated that implanted Si takes the form of extremely small a-Si nanoinclusions (see Secs. II C and II D). Two peaks were not distinguishable in the SHG spectrum. For the annealed 3 nm NC layers, the fit decomposed the SHG response into three interband resonances with resonance energies 3.50, 3.87, and 4.89 eV [annealed in Ar, Fig. 8(b)] or 3.50, 3.84, and 4.90 eV [annealed in Ar/H$_2$, Fig. 8(c)]. The weak 3.5 ± 0.1 eV resonance, though not directly discernible as a peak or shoulder, accounts for the low-energy wing of the $\Gamma_{NC}(\hbar\omega_{SH})$ spectra, and corresponds closely in energy to the low-energy shoulder (3.34 ± 0.02 eV) observed in the PLE spectrum [Fig. 1(c)] of this sample. The emergence of this resonance from the fit suggests the presence of a weak E_1-like CP transition that was not evident from casual inspection of the SHG spectrum. For the 5 nm NC layer, the fit decomposed the SHG response into three resonant contributions at energies 3.41, 3.73, and 4.80 eV [see Fig. 8(d)]. All three resonances are discernible as prominent peaks in the data. These energies are redshifted by ~0.1 eV from the corresponding fitted resonances of the 3 nm NC layer. On the other hand, they are *blue* shifted from the three prominent fitted resonances (3.34, 3.60, and 4.39 eV) of the SHG spectrum of a *planar* Si(001)/SiO$_2$ interface.[39] Possible physical origins of these resonances are discussed in Sec. IV.

The solid curves in the right-hand panels of Fig. 8 show reconstructions of the SHG phase spectra $\Phi(\hbar\omega_{SH})$ based on Eq. (7), and are derived from the same parameters used to fit the corresponding amplitude spectra in the left-hand panels. The good agreement between the experimental and reconstructed phase spectra confirms the Kramers-Kronig relation between the SHG amplitude and phase spectra.

D. XP2-SFG spectrum

The analysis of Sec. III C tacitly assumed that resonances observed in SHG spectra occurred when the SH photon energy $\hbar\omega_{SH}$ matched material transitions at $\hbar\omega_k$. However, resonances can also occur at the fundamental photon energy $\hbar\omega$. To distinguish these two possibilities, we acquired a partial XP2-SFG spectrum of the 5 nm NC sample. For XP2-SFG, a fixed-wavelength 800 nm ($\hbar\omega_1 = 1.55$ eV) pulse train combined in the sample with the orthogonally polarized tunable NOPA pulse train. The quadrupolar SFG polarization densities are

$$\vec{P}_{NC}^{(2)}(\omega_1 + \omega_2) = \left|\Gamma_{NC}^{(SFG)}\right|e^{i\Phi_{SFG}}[\vec{E}_1(\omega_1) \cdot \nabla]\vec{E}_2(\omega_2), \tag{8}$$

$$\vec{P}_g^{(2)}(\omega_1 + \omega_2) = \Gamma_g^{(SFG)}[\vec{E}_1(\omega_1) \cdot \nabla]\vec{E}_2(\omega_2), \tag{9}$$
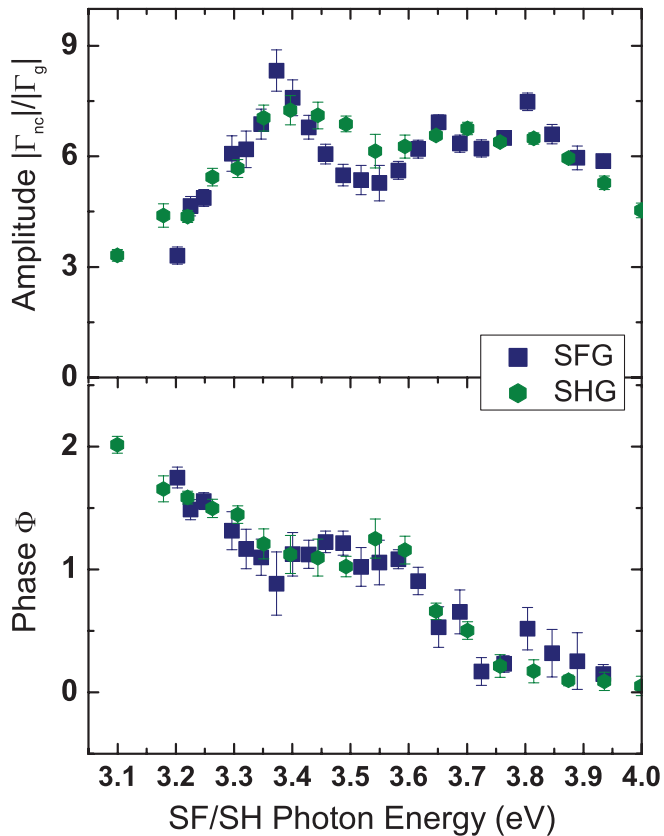
FIG. 9. (Color online) SFG normalized amplitude (upper panel) and phase (lower panel) spectra of 5 nm Si NC sample (filled blue square data points) plotted vs $\hbar\omega_{SF}$, compared with the corresponding SHG spectra (filled olive circle data points) plotted vs $\hbar\omega_{SH}$.

for NC layer and substrate, respectively, where $|\Gamma_{NC}^{(SFG)}|$ and $\Gamma_g^{(SFG)}$ are amplitudes of the SFG polarization densities, Φ_{SFG} is the phase difference between them, and ω_2 denotes the tunable NOPA pulse frequency. Data was collected and analyzed as for XP2-SHG.

The blue filled squares in Fig. 9 present the measured SFG amplitude (upper panel) and phase (lower panel) of the 5 nm NC sample vs summed photon energy $\hbar(\omega_1 + \omega_2)$. The filled olive circles show the corresponding SHG amplitude (upper) and phase (lower) vs $\hbar\omega_{SH}$. Within experimental error, the SFG and SHG spectra are identical. The two resonant features shown occur at the same summed photon energy $\hbar\omega_{SH} = \hbar(\omega_1 + \omega_2) = 3.4$ and 3.7 eV in both spectra, proving that they were at $\hbar\omega_{SH} = 3.4$ and 3.7 eV, rather than $\hbar\omega = 1.7$ and 1.85 eV in the SHG spectra. This result is of special importance because of the known presence of strong optical transitions at approximately half the energy of the 3.4 eV transition—namely, those responsible for the PL shown in Fig. 1(b).

In order to check the resonance around 4.8 eV, XP2-SFG spectra were obtained on the 3 nm Si NC samples in the range $4.8 \leqslant \hbar\omega_{SF} \leqslant 5.1$ eV, using tunable NOPA pulses and frequency-doubled (400 nm) fundamental pulses. Strong absorption of the SFG signal in this extended range in the 5 nm Si NCs prevented spectroscopic study in that sample. The 400 nm + NOPA XP2-SFG results for 3 nm samples are

shown in Figs. 8(b) and 8(c). The resonance at 4.9 eV appears prominently in the left-hand panels of these figures, and agrees well with the model fitting (solid curves).

IV. DISCUSSION

Acquisition of parallel PLE, SE, and SHG/SFG spectra from common Si NC samples facilitates identification and interpretation of resonant features, and highlights similarities and differences among the complementary spectroscopies. In Secs. IV A and IV B we discuss these similarities and differences in detail. In Sec. IV C we discuss a physical interpretation of the intermediate 3.8 eV resonance that emerges from this comparison. In Sec. IV D we calculate the SHG spectra from $\varepsilon(\omega)$ determined by SE, using a model developed by Mochan *et al.*[43] that treats each NC as a dielectric sphere comprised of a continuous distribution of polarizable entities, each responding nonlinearly to the gradient of the incident field as a forced harmonic oscillator. Though crude, this exercise helps distinguish those features of SHG that are derivable from knowledge of the linear spectra from those that convey additional information. In particular, the anomalous blueshift of the E_2-like SHG resonance follows naturally from this model, whereas the anomalous strength of the intermediate 3.8 eV resonance and the high sensitivity of spectral structure to NC size appear to be unique SHG features.

A. Similarities among PLE, SE, and SHG/SFG spectra

Here we emphasize three recurring features among the PLE, SE, and SHG/SFG spectra presented in Secs. II and III. First, among the annealed (Si NC) samples, three resonances appear with remarkable consistency in the spectral range from 3 to 5 eV: two at energies near the E_1 and E_2 CPs of bulk c-Si, and a third with no bulk c-Si counterpart at an energy between E_1 and E_2. In some cases—specifically SE [Figs. 3(f) and 3(g)] and SHG [Figs. 8(b) and 8(c)] spectra of 3 nm Si NC samples—the E_1-like peak is discernible only as an extended low-energy tail on higher-energy features. Its existence in these cases must be inferred indirectly from fits of the data to oscillator models. Nevertheless, the unambiguous presence of an E_1-like peak in the PLE spectra of 3 nm Si NCs [Fig. 1(c)] and in all spectra of 5 nm Si NCs lends credence to its existence in these ambiguous cases. In all other cases, all three peaks are discernible directly in the raw data.

Second, certain characteristics of these three resonant peaks recur in all or nearly all of the spectroscopic data. For example, the E_2-like peak is consistently stronger than the E_1-like peak in PLE, SE, and SHG spectra of both 3 and 5 nm Si NC samples. This is also true of bulk c-Si, although in nearly all cases the E_2/E_1 ratio is much larger in the spectra of Si NCs than for bulk c-Si. The lone exception is the SHG spectrum of 5 nm NCs, where the ratio is approximately the same as for bulk c-Si. As another example, the E_1-like peak, when clearly resolved, appears at a remarkably consistent energy of 3.3–3.4 eV in all three types of spectra. The intermediate peak is consistently the broadest peak in all spectra. As a final example, all three types of spectra are insensitive in most respects to whether the sample was annealed in Ar or in Ar/H_2 mixture [Figs. 3(f) and 3(g);

Figs. 8(b) and 8(c)] despite the strong effect of hydrogen on PL intensity [Fig. 1(a)]. Recently, Gevers *et al.* reported that SHG in the spectral range $1.6\,\text{eV} < \hbar\omega_{\text{SH}} < 3.5\,\text{eV}$ from a planar c-Si surface covered with a thin a-Si film created by Ar^+-ion bombardment of H-terminated Si(100) originates predominantly from interface-modified E_0'/E_1 CP transition in c-Si.[58] Such dominance of CP electronic transitions over interface bonds is consistent with the insensitivity to the forming gas in our spectra. One exception is noted in the next section. Relative amplitudes and energies of the three resonant peaks are evidently insensitive to H passivation of interfacial defects.

Third, SE and SHG yield mutually consistent spectra of the as-implanted sample [Figs. 3(a), 3(e), and 8(a)]. Some substructure is evident in SE that is not resolved in SHG, but the average energy (∼4.5 eV) and width (FWHM ∼1.8 eV) of the composite spectral peak is consistent between the two spectra. Because of its extremely weak PL intensity, no PLE spectrum could be acquired for the as-implanted sample.

B. Differences between linear (PLE, SE) and SHG/SFG spectra

Despite similarities, significant differences in the properties of the three resonant structures are also observed between linear (PLE, SE) and SHG spectra of the annealed Si NC samples. First, there are significant differences in the relative strength (amplitude × width for PLE and SE spectra, and amplitudes f_k for SHG) of the E_1-like feature. In SE [$\varepsilon_2(\omega)$] and PLE, E_1 is consistently three to six times weaker than the other two resonances for all annealed samples [Figs. 3(f)–3(h) and Table I]. E_1 appears relatively weaker in the SHG spectra of 3 nm Si NCs [Figs. 8(b), 8(c), and Table I], where its existence can be inferred only indirectly from fitting and by comparison to the PLE spectrum. On the other hand, in the SHG spectrum of 5 nm Si NCs, the E_1-like feature becomes as strong as the intermediate and E_2-like resonances [Fig. 8(d)]. The latter behavior is anomalous even compared to SHG spectra of planar Si(001)/SiO$_2$ (Ref. 39) and Si(111)/SiO$_2$ (Ref. 57) interfaces, where the E_1-like resonance, though prominent, is generally weaker than the E_2-like resonance.

Second, similar remarks apply to the intermediate peak. The intermediate peak completely dominates the SHG spectrum of 3 nm NCs, whereas it is comparable in strength (amplitude × width) to E_2 in PLE and SE of these samples. The fitted width of this resonance in SHG spectra decreases noticeably from ∼1 eV for 3 nm NCs annealed in Ar to ∼0.6 eV for those annealed in Ar/H$_2$. This is the single most noticeable effect of hydrogen in any of the spectra. The width decreases further to ∼0.3 eV for 5 nm samples (see Table I). By contrast, in PLE and SE spectra of 3 nm NCs this resonance is unaffected by hydrogen, and narrows only slightly from ∼0.8 to ∼0.6 eV in going from 3 to 5 nm NCs. The fitted energy of this resonance is also consistently slightly lower (3.7 – 3.9 eV) in SHG spectra than in PLE and SE (3.9 – 4.0 eV). These variations suggest that the intermediate resonance may arise from a variety of Si/SiO$_2$ interfacial structures to which PLE and SE on the one hand, and SHG on the other, show different sensitivity, as discussed further in the next section.

Third, the E_2-like resonance appears at anomalously high energy (4.8–4.9 eV) in all SHG/SFG spectra compared to the 4.4–4.7 eV peak observed in PLE and SE. This apparent discrepancy will be resolved in Sec. IV D.

Finally, the SHG spectra exhibit far greater contrast in all respects between the 3 and 5 nm Si NC samples than the PLE and SE spectra. Not only is the spectrally averaged SHG amplitude $\Gamma_{\text{NC}}^{(5\,\text{nm})}$ approximately 10 times stronger per NC than $\Gamma_{\text{NC}}^{(3\,\text{nm})}$, the SHG spectral structure changes markedly from the 3 nm samples to the 5 nm sample. The featureless nature of the former spectrum, which is dominated by the broad 3.9 eV intermediate peak [Figs. 8(b) and 8(c)], transforms to a featured spectrum with three strong resonant peaks [Fig. 8(d)]. In stark contrast, the PLE and SE spectra show only subtle differences in overall amplitude and spectral structure between the 3 and 5 nm samples [Figs. 1(c) and 3(f) – 3(h)].

C. Physical interpretation of the optical resonances

Daum and co-workers previously observed spectral structures intermediate in energy between the E_1 and E_2 resonances in SHG spectroscopy of planar Si(001)/SiO$_2$ (Ref. 39) and Si(111)/SiO$_2$ (Ref. 57) interfaces. However, such structures have not previously, to our knowledge, been correlated with corresponding structures in linear spectra. At planar Si(001)/SiO$_2$, a peak ranging in energy from 3.68 to 3.77 eV (depending on oxidation procedure) with FWHM ∼0.5 eV was observed.[39] The dependence of both peak energy and amplitude on oxidation procedure demonstrated the interfacial nature of the resonance. This resonance was attributed to Si atoms at the interface between the substrate and its thin suboxide transition region that lack the T_d symmetry of the c-Si lattice. Its width was attributed to the range of bond angles and lengths at this interface.[39] At planar Si(111)/SiO$_2$ interfaces, an SHG peak at 3.52 eV (FWHM ∼0.3 eV) was observed, and also attributed to transitions localized in interfacial suboxide groups.[57] The appearance of such interfacial resonances in linear spectra of embedded Si NCs evidently reflects their high interface/volume ratio compared to planar Si/SiO$_2$ samples.

Since an embedded Si NC possesses nanointerfaces of all crystallographic orientations, the broad intermediate peak in the SHG spectra of Si NCs may be an inhomogeneous combination of intermediate peaks observed at planar Si(001)/SiO$_2$ and Si(111)/SiO$_2$ interfaces. There is evidence for this in our data. For example, the intermediate peak for 3 nm Si NCs—the strongest feature in the SHG spectrum of this sample—is broader (FWHM ∼1 eV for NCs annealed in Ar) than the analogous features observed at those planar interfaces. The intermediate peak is also broader in $\varepsilon_2(\omega)$ and PLE spectra (FWHM 0.6 − 0.8 eV) than in SHG spectra of planar Si/SiO$_2$ interfaces.[39,57]

An additional source of a broad intermediate resonance must, however, also be considered: a-Si. Indeed, $\varepsilon_2(\omega)$ of bulk a-Si exhibits a broad maximum between E_1 and E_2 of bulk c-Si [see dashed curve in Fig. 3(e)]. In their SHG studies of planar Si/SiO$_2$ interfaces, Daum and co-workers[39] rejected interfacial a-Si as a significant source of the strong intermediate SHG resonance on the grounds that spectroscopic SHG from a planar oxidized a-Si sample was far too weak and featureless [see Fig. 1 of Ref. 39] to account for it. In

the present study of embedded Si NCs, this argument must be reexamined for three reasons. First, Raman spectra (Fig. 4) provide strong evidence that residual a-Si is present even in the annealed samples (Sec. II D). Second, both $\varepsilon_2(\omega)$ [Fig. 3(e)] and Γ_{NC}/Γ_g [Fig. 8(a)] of the *as-implanted* sample—in which Raman spectroscopy shows that implanted Si takes the form of extremely small a-Si nanoinclusions—are *comparable* in magnitude to $\varepsilon_2(\omega)$ and Γ_{NC}/Γ_g of the annealed NC samples. Moreover, the blueshift of the peak spectral response of as-implanted nanoinclusions (~4.5 eV) from the intermediate peak of the Si NC spectra (3.7−3.9 eV) is consistent with a quantum confinement shift that is reduced or removed when the a-Si material redistributes within the larger volume of 3 to 5 nm Si NCs. Thus the ~4.5 eV peak observed from the as-implanted sample can be interpreted as a blue-shifted replica of the 3.7–3.9 eV intermediate peak observed from Si NC samples. Third, *ab initio*[15] and molecular dynamics[16] simulations have shown that Si NCs of a few nanometers diameter embedded in amorphous SiO_2 develop concentric transitional shells of a-Si and suboxide that surround the c-Si core. According to these simulations, the nanoparticle becomes completely amorphous below a threshold diameter of ~2 nm, consistent with our interpretation of Raman and optical spectra of the as-implanted sample. For $d_{NC} > 2$ nm, a c-Si core develops, and the a-Si shell thins with increasing diameter, eventually disappearing altogether. The latter prediction is consistent with our observation in SE [$\varepsilon_2(\omega)$] and PLE of a 25% decrease in the strength (amplitude × width) of the intermediate resonance relative to E_2, and in SHG of a modest 23% increase in the amplitude (f_k) of this resonance relative to E_2, in going from 3 to 5 nm NCs annealed in Ar/H_2 (see Table I). Considering that 5 nm NCs have $(5/3)^2$, or 278%, more surface area than 3 nm NCs, these results imply that the disordered Si shell thins by at least a factor of 2, assuming that $\varepsilon_2(\omega)$ and $\Gamma_{NC}(\omega)/\Gamma_g$ in this spectral range scale with the total amount of material in that shell. Of course, the observation that the intermediate peak scales somewhat differently in SE/PLE than in SHG shows that the latter assumption is too simplistic. Nevertheless, the results remain consistent with the predicted[15,16] thinning of the disordered Si shell.

We observe that the width of the intermediate resonance depends on both annealing and NC size. For 3 nm NCs, this resonance as observed in PLE and SE has the same width for samples annealed in Ar/H_2 and pure Ar, whereas in SHG it is 40% narrower for samples in annealed in Ar/H_2. This suggests that the peak is inhomogeneously broadened, and that hydrogen termination on the nanointerface eliminates some contributions to which SHG is uniquely sensitive. In all three types of spectra, the width of this resonance narrows on going from 3 to 5 nm NCs annealed in Ar/H_2, albeit more strongly in SHG (another 40%) than in PLE and SE (~20%). Since curvature and strain at the nanointerface decrease significantly from 3 to 5 nm NCs, the range of bond angles and lengths at this interface may narrow, thereby narrowing the inhomogeneous width of this resonance. Narrowing of this resonance with increasing NC size can then be interpreted as a transition to the narrower intermediate resonances observed at planar Si/SiO_2 interfaces.[39,57]

The most striking contrast between SHG and linear (SE, PLE) spectra is the far greater sensitivity of SHG to particle size and, to a lesser extent, to annealing treatment. This is true not only of the intermediate peak, but of the E_1 and E_2 resonances. This contrast provides empirical evidence that SHG is selectively sensitive to the nanointerfacial region of the embedded NCs, for two reasons. First, the nanointerface is the locus of size-dependent strain gradients, a significant source of SHG enhancement and of interface-modified critical-point resonances at planar Si/SiO_2 interfaces.[59] Variation of NC size provides a convenient means of varying interfacial strain that is not available at planar interfaces. Second, the nanointerface is the locus of size-dependent structural variations, such as size-dependent a-Si and suboxide transition regions predicted in simulations.[15,16] Interfacial strain gradients and structural discontinuities break centrosymmetry locally, and in a NC-size-dependent manner, and thus can selectively influence SHG spectra. We therefore propose that the nanointerfacial region provides a significant, if not dominant, contribution to the SHG spectra.

The pronounced appearance of the E_1 resonance for 5 nm NCs, and its suppression relative to E_2 for 3 nm NCs, observed to varying degrees in all three types of spectra in this work, is consistent with size-dependent trends observed in previous SE[25] and computational[53] studies of embedded Si NCs. The E_1 resonance in bulk c-Si owes much of its oscillator strength to electron-hole pair correlation (i.e., excitonic effect), which is reduced or eliminated in small NCs. The lost oscillator strength is transferred to higher-energy optical transitions.

D. Derivation of SHG spectrum from SE data

Mochan *et al.*[43] have shown that in certain simple approximations the second-harmonic response function $\Gamma_{NC}(\omega)$ of an array of centrosymmetric nanospheres can be expressed analytically in terms of its linear dielectric function $\varepsilon(\omega)$. Since $\Gamma_{NC}(\omega)$ and $\varepsilon(\omega)$ are both available experimentally from the present study, examination of this simple analysis is highly appropriate. The interior of each nanoparticle is treated as a continuous distribution of harmonic polarizable entities. The origin of the nonlinear response is the spatial variation of the driving field across each dipole.[60] Analytic expressions for the parameters γ^e, γ^m, and γ^q in Eq. (4) are given in Eqs. (B4)−(B6) of Ref. 43. Here γ^e, γ^m, and γ^q are expressed in terms of $\varepsilon(\omega)$ and three additional parameters that characterize the nonlinear response of the spherical interface of each nanosphere. Analytic expressions for these interface parameters are given in Eqs. (B8)−(B10) of Ref. 43. No explicit reference to the microscopic crystalline, amorphous, or interfacial structures of the nanosphere is made in this model. Rather microstructure is included implicitly by expressing $\Gamma_{NC}(\omega)$ in terms of $\varepsilon(\omega)$, which is a reflection of the underlying structure. Plots of the second-harmonic response function for a single Si nanosphere and for a uniform composite, using the $\varepsilon(\omega)$ of *bulk* c-Si, are presented in Figs. 7 and 8 of Ref. 43.

Figure 10 presents our analytic calculation of $\Gamma_{NC}(\omega)$ for the three annealed samples studied here, using the experimental $\varepsilon(\omega)$ shown in Fig. 3. For comparison, the corresponding SHG response function for a flat c-Si surface is also plotted (dotted line) using a continuum dipolium model for a flat surface.[60] Several features warrant comment. First, as in the
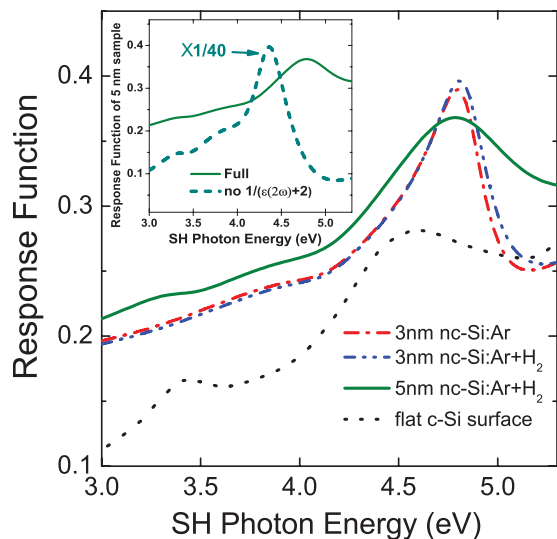
FIG. 10. (Color online) Normalized SHG response functions ($e\rho_{NC}/R_{NC}^3)\Gamma_{NC}(\omega)$ for each annealed sample calculated from their measured linear dielectric functions shown in Fig. 3 using a continuum dipolium model for spherical NC vs the photon energy, where ρ_{NC} is the NC density, R_{NC} is the radius of the NC and e is the elementary charge.[43] For comparison, the corresponding SHG response function ($|r_{pP}|$ from Eq. (1) of Ref. 61, erratum of Ref. 60) for a flat c-Si surface is also plotted (dotted line) using a continuum dipolium model for a flat surface (Ref. 60). The inset shows the same response function for the 5 nm sample (olive solid curve), and its corresponding value (dark cyan dashed curve) when the $1/[\varepsilon(2\omega)+2]$ screening factor is removed from its defining expression.

corresponding $\varepsilon_2(\omega)$ spectra in Fig. 3, the E_2 peak dominates in all cases. The other two peaks are clearly discernible only for the 5 nm NC case. Second, the E_1 and intermediate peaks, where discernible, appear within ± 0.1 eV of their corresponding positions in the SE spectrum. These similarities are expected, since the SE data is input to the calculation. Third, however, the E_2 peaks for the NCs occur at $\sim$4.8 eV, shifted about 0.4 eV to the blue from their positions in the corresponding $\varepsilon_2(\omega)$ spectra, but very close to their positions in the SHG spectra (see Table I and Fig. 8). Fourth, the E_2 peak for the flat c-Si surface occurs at $\sim$4.5 eV, very close to its position in the $\varepsilon_2(\omega)$ spectra.

As seen in Fig. 10, the SHG response function for a flat c-Si surface using the continuum dipolium model clearly shows E_1 and E_2 CPs with energy positions agreeing well with the reported experimental values for flat c-Si surfaces.[39,57] E_2 is only slightly blue shifted from the bulk CP values $[E_2(X) = 4.27$ eV; $E_2(\Sigma) = 4.52$ eV].[51] This shifting comes from the Fresnel factors that screen the incoming fundamental fields that generate the SH signal below the flat surface. For a NC, the screening factors corresponding to its spherical shape produce a much stronger blueshift than for the flat surface, as seen in Fig. 10. Thus the anomalous blueshift in E_2 in the SHG response for NCs, according to the dipolium model, is directly related to the screening factors for a spherical shape. E_1, on the other hand, is not shifted from the bulk CP value

($E_1 = 3.4$ eV) for either a flat Si surface or for spherical Si NCs.

Detailed analysis of the screening terms embedded in γ^e and γ^m—the dominant hyperpolarizabilities responsible for SHG from Si NCs[43]—shows that the E_2 blueshift originates from a factor $[\varepsilon(2\omega) + 2]^{-1}$ [see Eqs. (B4) and (B5) of Ref. 43] characteristic of the screening term for the dipolar electric field within the sphere. Here $\varepsilon(2\omega)$ denotes the dielectric function at the SH frequency. The much smaller E_2 blueshift for the flat Si surface originates from a corresponding factor $[\varepsilon(2\omega)]^{-1}$ in the screening term [see Eq. (2) of Ref. 61]. To demonstrate these origins, the inset of Fig. 10 plots the SH response for the 5 nm sphere when the factor $[\varepsilon(2\omega) + 2]^{-1}$ is removed. The E_2 blueshift is eliminated. A similar result is obtained for the 3 nm particle. Of course, other features of the response, such as the amplitudes and widths of the resonances, are also affected, but here we focus just on the peak positions. The reason that only E_2 blue shifts is explained by competing contributions of the E_2 and the nearby E_1' CP resonances to the crucial screening factors $[\varepsilon(2\omega) + 2]^{-1}$ and $[\varepsilon(2\omega)]^{-1}$ at SH photon energies immediately above 4.2 eV. E_1' comes from Λ-line transitions between the top valence band and the second-lowest conduction band, and occurs at 5.3 eV in bulk Si.[62,63] The competition between E_2 and E_1' contributions gives $[\varepsilon(2\omega) + 2]^{-1}$ a very different spectral shape than $[\varepsilon(2\omega)]^{-1}$ at photon energies between the two resonances, accounting for the E_2 blueshift. On the other hand, the E_1 resonance is separated by a much larger energy gap than E_2 from E_1', and is thus negligibly affected by E_1' contributions. Thus an E_1 shift is observed neither in the calculations in Fig. 10 nor in experiments.

While this calculation serves the limited purpose of explaining the apparent shift of the SHG E_2 resonance, it also shows that in most other respects the SHG spectrum is *not* derivable from SE. The relative strengths and widths of the three main peaks do not reflect their measured values in the SHG spectrum, nor is their any basis in this model for the unique sensitivity of SHG spectral structure to NC size and annealing treatment. It therefore reinforces the conclusion of the previous section that SHG probes nanointerfacial regions of embedded NCs more sensitively than SE.

V. CONCLUSION

XP2-SHG has been applied spectroscopically to study the oxide-embedded Si NCs of different sizes and interface chemistries. The SHG spectra response was compared in detail with results from complementary conventional spectroscopies to help elucidate the unique structure of the Si NCs. The appearance of bulklike CP resonances in the parallel PLE, SE, and SHG/SFG spectra from Si NCs suggests the basic electronic structure of the bulk c-Si is preserved in nanoparticles as small as 3 nm in diameter, albeit with significant size-dependent modification. At the same time, the prominence of a non-bulk-like resonance intermediate in energy between E_1 and E_2 CPs in all three types of spectra demonstrates the important contribution of nanointerfaces to the electronic structure. The dominance of the latter feature in SHG spectra of 3 nm NCs, and the unique sensitivity of SHG spectral structure and amplitude to NC diameter suggest that SHG is uniquely

sensitive to nanointerfacial structure. Thus quadrupolar SHG of nanocomposites, in its ability to reveal interfacial structure, appears to play a role analogous to dipolar SHG of planar interfaces. The comparative spectroscopy presented here leads to the hypothesis that this intermediate resonance may arise from Si/SiO_2 interfacial structures such as an a-Si/suboxide shell predicted in recent simulations.

*downer@physics.utexas.edu

[1] L. T. Canham, Appl. Phys. Lett. **57**, 1046 (1990).

[2] L. Pavesi, L. Dal Negro, C. Mazzoleni, G. Franzo, and F. Priolo, Nature (London) **408**, 440 (2000).

[3] R. J. Walters, G. I. Bourianoff, and H. A. Atwater, Nat. Mater. **4**, 143 (2005).

[4] D. Kovalev, H. Heckler, M. Ben-Chorin, G. Polisski, M. Schwartzkopff, and F. Koch, Phys. Rev. Lett. **81**, 2803 (1998).

[5] C. W. White, J. D. Budai, S. P. Withrow, J. G. Zhu, E. Sonder, R. A. Zuhr, A. Meldrum, D. M. Hembree Jr., D. O. Henderson, and S. Prawer, Nucl. Instrum. Methods Phys. Res. B **141**, 228 (1998); S. P. Withrow, C. W. White, A. Meldrum, J. D. Budai, D. M. Hembree Jr., and J. C. Barbour, J. Appl. Phys. **86**, 396 (1999).

[6] F. Koch and V. Petrova-Koch, J. Non-Cryst. Solids **198-200**, 840 (1996).

[7] M. V. Wolkin, J. Jorne, P. M. Fauchet, G. Allan, and C. Delerue, Phys. Rev. Lett. **82**, 197 (1999).

[8] X. X. Wang, J. G. Zhang, L. Ding, B. W. Cheng, W. K. Ge, J. Z. Yu, and Q. M. Wang, Phys. Rev. B **72**, 195313 (2005).

[9] M. Ippolito, S. Meloni, and L. Colombo, Appl. Phys. Lett. **93**, 153109 (2008).

[10] A. Puzder, A. J. Williamson, J. C. Grossman, and G. Galli, Phys. Rev. Lett. **88**, 097401 (2002).

[11] I. Vasiliev, J. R. Chelikowsky, and R. M. Martin, Phys. Rev. B **65**, 121302 (2002).

[12] R. J. Baierle, M. J. Caldas, E. Molinari, and S. Ossicini, Solid State Commun. **102**, 545 (1997).

[13] B. Garrido, M. Lopez, O. Gonzalez, A. Perez-Rodriguez, J. R. Morante, and C. Bonafos, Appl. Phys. Lett. **77**, 3143 (2000).

[14] S. Godefroo, M. Hayne, M. Jivanescu, A. Stesmans, M. Zacharias, O. I. Lebedev, G. Van Tendeloo, and V. V. Moshchalkov, Nat. Nanotech. **3**, 174 (2008).

[15] N. Daldosso, M. Luppi, S. Ossicini, E. Degoli, R. Magri, G. Dalba, P. Fornasini, R. Grisenti, F. Rocca, L. Pavesi, S. Boninelli, F. Priolo, C. Spinella, and F. Iacona, Phys. Rev. B **68**, 085327 (2003).

[16] F. Djurabekova and K. Nordlund, Phys. Rev. B **77**, 115325 (2008).

[17] A. Sakko, C. Sternemann, Ch. J. Sahle, H. Sternemann, O. M. Feroughi, H. Conrad, F. Djurabekova, A. Hohl, G. T. Seidler, M. Tolan, and K. Hamalainen, Phys. Rev. B **81**, 205317 (2010).

[18] C. M. Hessel, E. J. Kelly, R. G. Cavell, T. Sham, and J. G. C. Veinot, J. Phys. Chem. C **112**, 14247 (2008).

[19] M. Sykora, L. Mangolini, R. D. Schaller, U. Kortshagen, D. Jurbergs, and V. I. Klimov, Phys. Rev. Lett. **100**, 067401 (2008).

[20] J. P. Wilcoxon and G. A. Samara, Appl. Phys. Lett. **74**, 3164 (1999).

[21] D. Amans, S. Callard, A. Gagnaire, J. Joseph, G. Ledoux, and F. Huisken, J. Appl. Phys. **93**, 4173 (2003).

[22] B. Gallas, I. Stenger, C. C. Kao, S. Fisson, G. Vuye, and J. Rivory, Phys. Rev. B **72**, 155319 (2005).

[23] L. Ding, T. P. Chen, Y. Liu, C. Y. Ng, and S. Fung, Phys. Rev. B **72**, 125419 (2005).

[24] L. Ding, T. P. Chen, Y. Liu, M. Yang, J. I. Wong, Y. C. Liu, A. D. Trigg, F. R. Zhu, M. C. Tan, and S. Fung, J. Appl. Phys. **101**, 103525 (2007).

[25] A. En Naciri, M. Mansour, L. Johann, J. J. Grob, and H. Rinnert, J. Chem. Phys. **129**, 184701 (2008).

[26] M. I. Alonso, I. C. Marcus, M. Garriga, A. R. Goni, J. Jedrzejewski, and I. Balberg, Phys. Rev. B **82**, 045302 (2010).

[27] H. Xia, Y. L. He, L. C. Wang, W. Zhang, X. N. Liu, X. K. Zhang, and D. Feng, J. Appl. Phys. **78**, 6705 (1995).

[28] S. Hernandez, A. Martinez, P. Pellegrino, Y. Lebour, B. Garrido, E. Jordana, and J. M. Fedeli, J. Appl. Phys. **104**, 044304 (2008).

[29] I. Stenger, B. Gallas, B. Jusserand, S. Chenot, S. Fisson, and J. Rivory, Eur. Phys. J. Appl. Phys. **44**, 51 (2008).

[30] D. Barba, F. Martin, and G. G. Ross, Nanotechnology **19**, 115707 (2008).

[31] G. A. Kachurin, S. G. Yanovskaya, V. A. Volodin, V. G. Kesler, A. F. Leier, and M. O. Ruault, Semiconductors **36**, 647 (2002).

[32] J. F. McGilp, Phys. Status Solidi A **175**, 153 (1999).

[33] G. Lupke, Surf. Sci. Rep. **35**, 75 (1999).

[34] W. Daum, Appl. Phys. A **87**, 451 (2007).

[35] K. Pedersen, Phys. Status Solidi B **247**, 2002 (2010).

[36] R. W. Terhune, P. D. Maker, and C. M. Savage, Phys. Rev. Lett. **8**, 404 (1962).

[37] J. E. Sipe, V. Mizrahi, and G. I. Stegeman, Phys. Rev. B **35**, 9091 (1987).

[38] O. A. Aktsipetrov, I. M. Baranova, and Yu. A. Ilinskii, Sov. Phys. JETP **64**, 167 (1986).

[39] G. Erley and W. Daum, Phys. Rev. B **58**, R1734 (1998).

[40] T. Stehlin, M. Feller, P. Guyot-Sionnest, and Y. R. Shen, Opt. Lett. **13**, 389 (1988).

[41] J. I. Dadap, J. Shan, K. B. Eisenthal, and T. F. Heinz, Phys. Rev. Lett. **83**, 4045 (1999).

[42] V. L. Brudny, B. S. Mendoza, and W. L. Mochan, Phys. Rev. B **62**, 11152 (2000).

[43] W. L. Mochan, J. A. Maytorena, B. S. Mendoza, and V. L. Brudny, Phys. Rev. B **68**, 085318 (2003).

[44] Y. Jiang, P. Wilson, and M. C. Downer, Appl. Phys. Lett. **78**, 766 (2001).

[45] P. Figliozzi, L. Sun, Y. Jiang, N. Matlis, B. Mattern, M. C. Downer, S. P. Withrow, C. W. White, W. L. Mochan, and B. S. Mendoza, Phys. Rev. Lett. **94**, 047401 (2005).

[46] L. Sun, P. Figliozzi, Y. Q. An, and M. C. Downer, Opt. Lett. **30**, 2287 (2005).

[47] O. A. Aktsipetrov, V. O. Bessonov, A. A. Nikulin, Q. Gong, X. Huang, and K. Chen, JETP Lett. **91**, 66 (2010).

[48] M. Stutzmann, M. S. Brandt, M. Rosenbauer, J. Weber, and H. D. Fuchs, Phys. Rev. B **47**, 4806 (1993).

[49] V. P. Bondarenko, V. E. Borisenko, A. M. Doroteev, I. N. Germanenko, and S. V. Gaponenko, J. Appl. Phys. **75**, 2727 (1993).

[50] A. R. Forouhi, *Properties of Amorphous Silicon*, 2nd ed., edited by The Institute of Electrical Engineers, EMIS Data Reviews Series No. 1 (INSPEC, London, 1989), p. 320.

[51] E. D. Palik, *Handbook of Optical Constants of Solids* (Academic, London, 1985).

[52] K. Seino, F. Bechstedt, and P. Kroll, Nanotechnology **20**, 135702 (2009).

[53] H. Ch. Weissker, J. Furthmuller, and F. Bechstedt, Phys. Rev. B **65**, 155328 (2002).

[54] A. Wirth, J. Wei, J. J. H. Gielis, P. Figliozzi, J. Rafaelsen, Y. Q. An, and M. C. Downer, Phys. Status Solidi C **5**, 2662 (2008).

[55] N. Bloembergen, R. K. Chang, S. S. Jha, and C. H. Lee, Phys. Rev. **174**, 813 (1968).

[56] T. Wilhelm, J. Piel, and E. Riedle, Opt. Lett. **22**, 1494 (1997).

[57] S. Bergfeld, B. Braunschweig, and W. Daum, Phys. Rev. Lett. **93**, 097402 (2004).

[58] P. M. Gevers, J. J. H. Gielis, H. C. W. Beijerinck, M. C. M. van de Sanden, and W. M. M. Kessels, J. Vac. Sci. Technol. A **28**, 293 (2010).

[59] W. Daum, H. J. Krause, U. Reichel, and H. Ibach, Phys. Rev. Lett. **71**, 1234 (1993).

[60] B. S. Mendoza and W. L. Mochán, Phys. Rev. B **53**, 4999 (1996).

[61] B. S. Mendoza and W. L. Mochán, Phys. Rev. B **61**, 16243 (2000).

[62] D. E. Aspnes and A. A. Studna, Phys. Rev. B **27**, 985 (1983).

[63] P. Lautenschlager, M. Garriga, L. Viña, and M. Cardona, Phys. Rev. B **36**, 4821 (1987).